Estuaries and Coasts (2025) 48:176
https://doi.org/10.1007/s12237-025-01605-1

Fortnightly Switching of Residual Flow Drivers Produced by Seawater Intrusion in a Long, Non-rotating Estuary

Erwan Garel[1] · Maziar Khosravi[1] · Manuel Díez-Minguito[2] · Arnoldo Valle-Levinson[3]

Received: 14 January 2025 / Revised: 8 August 2025 / Accepted: 11 August 2025 / Published online: 20 September 2025

Abstract

Towed and moored ADCP and salinity measurements were collected in Summer 2023 at two cross-channel transects of the 80-km-long Guadiana Estuary, at 4 km and 20 km from the mouth, during low (< 10 m^3/s) river discharge conditions. The dataset indicates that the lateral structure of axial residual flows changed from vertically sheared to laterally sheared with tidal forcing. These structures resemble theoretical expectations for a density-driven or eddy viscosity-shear covariance (ESCO) circulation at neap tide and for a tidally driven circulation produced by longitudinal advection (tidal stress) at spring tide. The tidal variability of the residual flow magnitude and of the contributions of unidirectional or two-layer vertical profiles indicate that the primary driver of the residual circulation changes between neap tide and spring tide. Seawater (i.e. with salinity > 35 kg/g) intrusion was several kilometres, equivalent to $\sim 1/8$ of the estuary's length. As a result, the horizontal density gradient was weakest near the mouth where the residual circulation was barotropic, produced by tidal stress at spring tide and possibly by an ESCO mechanism at neap tide. At 20 km upstream, the dominant driver switched from tidal stress at spring tide to a baroclinic (and potentially ESCO) circulation at neap tide. At this location, scaling analyses of the tidally averaged momentum equation using the densimetric tidal Froude number supported the idea of dominance of tidal stress at spring tide.

Keywords ADCP · Baroclinic · Barotropic · Tidal Froude number · Low river discharge

Introduction

Residual flows play a key role for a range of ecological, physical, and biogeochemical processes in estuaries, as they govern the along-channel (axial) net transport of suspended and dissolved material (e.g. Geyer & MacCready, 2014). Neglecting wind forcing, the residual circulation arises from the interplay between barotropic (tidally driven) and baroclinic (density-driven) forces (Burchard & Hetland, 2010; Li et al., 1998; Valle-Levinson, 2021). Baroclinic forcing stems from along-channel density gradients, which generate pressure gradients that drive the estuarine circulation. In contrast, barotropic processes encompass a variety of mechanisms that do not directly depend on density gradients, including eddy viscosity-shear covariance (ESCO) effects (Dijkstra et al., 2017), flow curvature (Chant, 2002), wind stress (Scully et al., 2005), tidal stresses (Li & O'Donnell, 2005), and Earth's rotation (Lerczak & Geyer, 2004).

At a given cross-section, the axial residual circulation may exhibit vertical shear, lateral shear, or a combination of both, often with asymmetries in its lateral distribution influenced by bathymetry, wind and Coriolis effects (e.g. Arnott et al., 2012; Burchard et al., 2011; Huijts et al., 2009; Huntley & Ryan, 2018; Valle-Levinson & Schettini, 2016; Valle-Levinson et al., 2000a, 2003, 2009; Wei et al., 2021; Winant & Gutiérrez de Velasco, 2003). Observations from long-term moorings and repeated cross-channel tidal surveys show that, while the strength of residual flows is generally modulated by tides, their spatial structure remains qualitatively unchanged in the absence of major changes in other external forcings such as river discharge, wind, or bathymetry (e.g. Basdurak & Valle-Levinson, 2013; Chawla et al.,

Communicated by Isabel Jalon-Rojas

✉ Erwan Garel
egarel@ualg.pt

[1] CIMA/ARNET, University of Algarve, Faro, Portugal

[2] Andalusian Institute for Earth System Research, University of Granada, Granada, Spain

[3] Civil and Coastal Engineering Department, University of Florida, Gainesville, USA

2008; de Jonge, 1992; Geyer et al., 2000; Kim & Voulgaris, 2005; Murphy et al., 2009; Reyes & Valle-Levinson, 2013; Scully & Friedrichs, 2007; Valle-Levinson et al., 2019). Theoretical analyses have also indicated that the transverse distribution of residual inflows and outflows depends on the dominant driver and on the estuary geometry (e.g. Burchard et al., 2011; Cheng & Valle-Levinson, 2009; Huijts et al., 2009; Lerczak & Geyer, 2004; Valle-Levinson, 2008; Wei et al., 2021; Winant, 2004, 2008). A persistent transverse structure of the residual circulation is therefore an indicator of a steady, dominant forcing.

In many midlatitude estuaries, the residual circulation typically consists of an inflow near the bed and outflow near the surface (Geyer & MacCready, 2014). Classical interpretations from pioneering studies attribute this pattern to a gravitational (baroclinic) circulation driven by the balance between the pressure gradient and bottom friction (Hansen and Rattray Jr. 1966; Pritchard, 1956). In estuaries with pronounced lateral slopes, the vertically sheared exchange flow transforms to laterally sheared due to frictional effects, with inflow in the deep channel and outflow over shallow areas (Fischer, 1976; Kasai et al., 2000; Wong, 1994).

Several studies have recently indicated that the ESCO circulation can also contribute to — or even dominate — the estuarine circulation in tidally energetic, well-mixed, or partially stratified estuaries (Burchard & Hetland, 2010; Cheng et al., 2010; Dijkstra et al., 2017; Jay & Musiak, 1994; Stacey et al., 2008). The strength and direction of residual flows produced by the various mechanisms are sensitive to factors such as the phase of eddy viscosity tidal variations, stratification, salinity distribution, wind, bathymetry, and freshwater inputs (Burchard & Hetland, 2010; Burchard & Schuttelaars, 2012; Burchard et al., 2011; Cheng et al., 2010, 2013; Dijkstra et al., 2017; Jay & Musiak, 1994; Stacey et al., 2008; Wei et al., 2021). In general, modelling studies and observations indicate that the ESCO mechanisms shape residual flows in a similar manner as baroclinic processes, at least at long estuaries (e.g. Burchard & Hetland, 2010; Cheng et al., 2010; Dijkstra et al., 2017; Stacey et al., 2008).

Barotropic forcings described by tidally averaged dynamics may also generate distinctive residual flow structures. For example, at dynamically short (i.e. with length < 0.6 times the tidal quarter-wavelength) and shallow estuaries where the residual circulation is driven exclusively by tides, the longitudinal advective flux of momentum (tidal stress) can produce a laterally shear exchange flow with inflow in the deep channel (Li & O'Donnell, 2005). An opposed barotropic exchange flow (outflow in the channel and inflow over the shoals) characterizes the seaward half (approximately) of systems with propagating (or progressive) tidal wave (Li & O´Donnell, 1997; Li & O'Donnell, 2005).

The distinction of the dominant driver of residual flows based on their lateral structure can be challenging, as different mechanisms may yield similar patterns. Nevertheless, observations indicating a periodic variability of the residual circulation at a fortnightly time scale suggest that the dominant driver varies with tidal forcing alone at some settings. For example, during the dry season, the residual flow structure at the Mossoró estuary (Brazil) is vertically sheared during neap tides and laterally sheared during spring tides, which is consistent with theoretical expectations for density-driven and tidally driven flows, respectively (Valle-Levinson & Schettini, 2016). A similar behaviour has been reported at the mouth of the semi-arid Guadiana Estuary, where a residual outflow throughout the water column at spring tides becomes vertically sheared at neap tides in the deep channel (Garel & Ferreira, 2013). However, the observations at the Guadiana Estuary lacked lateral resolution to resolve the cross-channel structure of the residual flow.

Extending previous observations in the Guadiana Estuary, this study investigates the lateral structure of the residual circulation using extensive (towed and moored) ADCP surveys at the middle and lower estuary. The aim is to show that the spatial pattern of residual flows can vary with tidal forcing over a fortnight in response to a switch in the dominant driver. It is argued that baroclinic and ESCO mechanisms, prevailing during neap tides, may be overwhelmed by tidal stresses during spring tides in estuaries where the horizontal salinity gradient is weakened by seawater intrusion.

Material and Methods

Study Area

The Guadiana is an 80-km-long estuary in Southern Iberia with a semi-arid Mediterranean climate (Fig. 1a). The estuary displays a trumpet shape, with a width of 1500 m at the mouth (i.e. at the seaward tip of a jetty), narrowing quickly to 700 m over the first 2 km upstream, and then more slowly to 70 m at the head. Intertidal areas with total surface area of about 20 km^2 are located at the lower estuary (Garel, 2017). The largest (about 10 km^2) is the Ayamonte salt marsh, on the eastern margin (Fig. 1a), which is also connected directly to the sea through a secondary inlet (Carreras) located further east (Morales, 1997; Morales & Garel, 2019). Along the estuary, the flow is confined to a single, relatively deep channel, meandering from one margin to the other. At the estuary's seaward half, the maximum depth is generally between 7 and 11 m (referred to mean sea level, hereafter) and the cross-section mean depth is between 4 and 9 m (Garel & Cai, 2018).

Tides in the region are semidiurnal with an average range of 1.3 m (microtidal) at neap tide and of 2.6 m (mesotidal) at spring tide. The maximum range is 3.4 m. A small diurnal inequality is noticeable at spring tide,

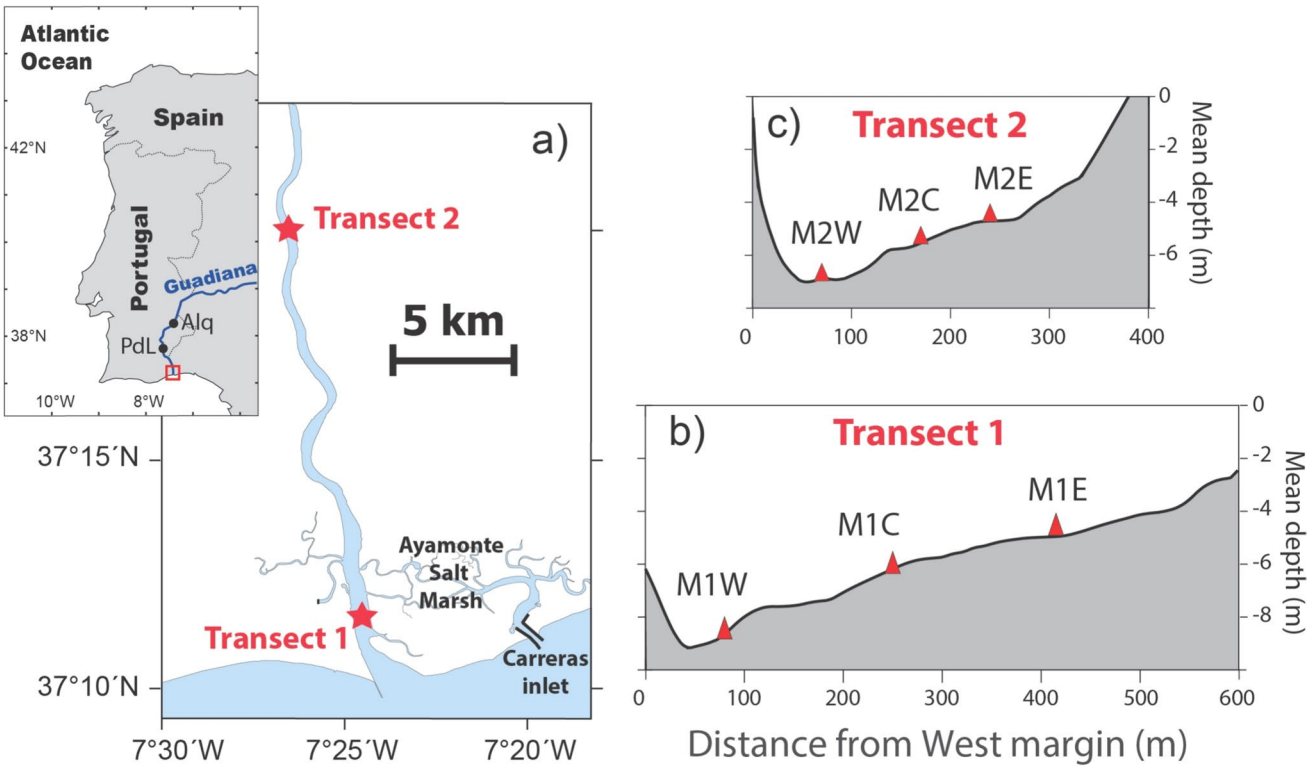

Fig. 1 **a** Location of the two surveyed transects (red stars) at the Guadiana Estuary (for general location, see inset, red area; PdL, Pulo de Lobo hydrographic station; Alq, Alqueva dam); bathymetric cross-sections at Transects 1 (**b**) and 2 (**c**) with location of the bed moorings (red triangles)

mainly, representing less than 10% of the semidiurnal signal (Garel & Ferreira, 2013). The tidal wave propagating along the channel has a progressive component and an approximately constant amplitude due to morphological convergence landward and reflection at the estuary head (Garel & Cai, 2018).

The freshwater discharge into the estuary is regulated by the Alqueva dam, the largest artificial dam in Southwest Europe, located at 60 km upstream from the estuary head across the Guadiana River. Water storage in reservoirs is prioritized in this semi-arid region subject to month-long periods of drought. Thus, the river discharge at the Guadiana Estuary is typically low, between 3 m^3/s (the minimum imposed value to maintain an ecological flow in the estuary) and 50 m^3/s. Moderate to high freshwater inflows (up to 2500 m^3/s) may occur during seldom water releases from the dam (every 2–4 years) or rain events, mostly in winter and spring. However, in summer, the freshwater discharge into the estuary is < 10 m^3/s (for details, see Garel & D'Alimonte, 2017). During a single tidal cycle, this discharge rate corresponds to a volume of freshwater input approximately 70 times lower than the average tidal prism (30 Mm^3; Correia et al., 2020). Under these conditions, the estuary is well-mixed, with periodic partial stratification developing on the ebb of neap tides (unpublished data).

Near the mouth, the residual circulation in the deep channel consists of an outflow at spring tide and a vertically sheared exchange flow at neap tide (Garel & Ferreira, 2013). This circulation pattern is related to tidal asymmetries, with longer and stronger (depth-averaged) currents during the ebb at spring tide and during the flood at neap tide. As a result, the net water transport direction reverses at intermediate tidal amplitudes (around 1 m, approximately). Cross-channel surveys performed near the mouth during dry conditions showed a residual outflow across the entire section (Teodósio & Garel, 2015), which might episodically be altered by the development of a near-bed inflow at the deep channel (Correia et al., 2020). The present study addresses this variability based on extensive ADCP surveys across the channel.

Data Acquisition

Data were collected in Summer 2023 simultaneously along two cross-channel transects, at 4 km and 20 km from the mouth (Fig. 1a). These locations were selected as they provide contrasted along-channel salinity gradients (typically strongest at the upstream location) but similar tidal forcings (see Garel & Cai, 2018). The near-mouth site corresponds to the location of previous ADCP measurements in the deep channel reporting a switch in the residual circulation between

neap and spring tides (Garel & Ferreira, 2013). The thalweg is close to the western margin at both locations. Transect 1, near the mouth, is 9 m deep at maximum and 600 m wide, while Transect 2, upstream, is shallower (7 m at maximum) and narrower (400 m; Fig. 1b, c). At each transect, three tripods of 0.5 m in height were moored at the bed for 2 months (July 14–September 21) at deep, intermediate, and shallow water depths. These moorings are hereafter identified based on their transect number and cross-channel location with W: West; C: Centre; and E: East (e.g. M1E refers to the eastern mooring of Transect 1; see Fig. 1b, c). M1W was raised by 0.7 m on July 24 (without record interruption) to avoid sand burying by migrating sand dunes reported by divers.

Each tripod was equipped with one upward-pointing ADCP, configured to provide ensemble averages every 15 min with standard deviations < 0.7 cm/s in bins of 0.2 to 0.5 m (Table 1). M2C operated for 41 days, only, as it overturned on August 25. M1E was temporally tilted on July 24, resulting in a 1-day data gap. This study also includes records at 1 min interval from CTD probes installed on moorings M1E (Seabird SMP37) and M2E (Seabird SBE19v2).

The moored records were complemented by towed ADCP surveys across the channel, performed simultaneously during 24 h at both transects using two boats. A WorkHorse II Monitor (1200 kHz) with cell size of 0.25 m was used at Transect 1; a Sentinel V20 (1000 kHz) with cell size of 0.4 m recorded data at Transect 2. The surveys were performed at neap tide (July 27–28, tidal amplitude of 0.6 m) and at spring tide (August 03–04, tidal amplitude of 1.5 m).

Moreover, salinity profiles were measured with a Valeport miniCTD every 2 km along the channel on 11 July 2023, i.e. 3 days before the moorings deployment when the tidal amplitude at the mouth was 0.75 m. These measurements were conducted with a fast boat following the high-water slack (at ~ 10 knots), from the mouth up to the salinity intrusion limit (i.e. where salinity < 1 g/kg).

The daily averaged river discharge was measured at the Pulo de Lobo hydrographic station, located at about 20 km from the estuary head (Fig. 1, inset). The last peak in river discharge before the survey occurred as a short (1 day) pulse on 2 March 2023 (142 m^3/s). Wind conditions were typical of the thermal breezes that affect the region in summer. Fair southerlies in the afternoon alternated with stronger northerly of maximum velocity between 4 and 8 m/s during the night. Potential wind effects on the residual circulation are likely negligible and not considered in the present study.

Residual Velocity and Tidally Average Salinity

The ADCP ensembles from the moorings were interpolated at intervals of 0.04 along the normalized water depth (with 0 = bed, 1 = surface). Only the data between the normalized intervals of 0.22 and 0.92 (depending on the instrument; see Table 1) were further analysed to discard most of the time gaps resulting from the ADCP blanking distance and side lobe effects. The north and east components of the current velocities were rotated in the along-channel component v (m/s, positive up-estuary) based on the angle of maximum variance of the flow (which was equal to the channel orientation). The residual velocity and tidal average salinity from moorings were obtained using a low-pass Butterworth filter of 80-h cut-off period, to remove the diurnal, semidiurnal, and lower-periods oscillations. The intensity of the residual

Table 1 Name, location, and configuration of the ADCP moored at Transects 1 and 2

Mooring	M1W	M1C	M1E	M2W	M2C	M2E
Location	Transect 1 West	Transect 1 Centre	Transect 1 East	Transect 2 West	Transect 2 Centre	Transect 2 East
Longitude Latitude	7° 24.725′W 37° 11.572′N	7° 24.616′W 37° 11.585′N	7° 24.508′W 37° 11.594′N	7° 26.531′W 37° 19.958′N	7° 26.456′W 37° 19.943′N	7° 26.397′W 37° 19.933′N
Mean water depth (m)	9.2 Deep	6.2 Intermediate	4.6 Shallow	6.6 Deep	6.2 Intermediate	4.5 Shallow
ADCP	TRDI WH 600 kHz	TRDI Sentinel V20	TRDI Sentinel V20	TRDI WH 600 kHz	TRDI WH 600 kHz	Nortek Signature 1000
Ensemble interval (min)	15	15	15	15	15	15
Cell size (m)	0.5	0.25	0.25	0.5	0.5	0.2
Standard deviation of velocity error (cm/s)	0.68	0.66	0.66	0.41	0.68	0.44
Blanking distance (m)	0.6	0.4	0.4	0.5	0.5	0.2
Fraction of the water column analysed	0.32–0.86	0.26–0.84	0.36–0.88	0.34–0.92	0.38–0.84	0.22–0.84

circulation at the moorings was quantified with the root mean square (rms) of the residual velocity profiles (Lerczak & Geyer, 2004).

The 10-s-averaged towed ADCP records were quality checked and processed following Valle-Levinson (2024). The validated axial velocities were gridded with (depth-normalized) vertical resolution of 0.1 and cross-channel resolution of 50 m. The residuals at each grid node were then obtained with least square fits to tidal harmonics, considering the D_1, D_2, D_3, D_4, and D_6 tidal bands (e.g. Valle-Levinson, 2022; Valle-Levinson & Atkinson, 1999). The mean coefficient of determination of the fits was > 0.9 for each of the four tidal surveys.

The tidally averaged (i.e. subtidal) salinity distribution on July 11 was estimated by shifting downstream the observations at high-water slack by half the tidal excursion (Savenije, 2012). The tidal excursion was computed as VT/π, where T is the tidal period (12.4 h) and V is the section mean, axial tidal current amplitude at Transect 1. V was computed as the velocity amplitude at M1W (deep channel) Weighted by a factor of 0.8. The latter factor was established in previous studies (Garel & D'Alimonte, 2017) and confirmed by the section mean current amplitudes obtained from the harmonic fits of the towed ADCP data. The tidal current amplitude at the moorings was computed as the mean of the three (flood-ebb-flood) peaks of absolute, vertically averaged, axial velocities occurring during each tidal cycle.

Barotropic and Baroclinic Flow Components

Two methods were used to separate the barotropic and baroclinic components from the residual ADCP signal. For mooring data, a principal component analysis (PCA) was applied to the vertical profiles of residual velocity to identify the contributions of the barotropic boundary layer (unidirectional vertical velocity profile) and baroclinic exchange flow (two-layer vertical velocity profile) to the temporal variability of the subtidal circulation (e.g. Stacey et al., 2001). The method was previously successfully applied at the Guadiana using data from an ADCP moored near M1W (see Garel & Ferreira, 2013). In the present study, the PCA was applied to the concatenated ADCP time series at each transect to elucidate the fortnightly variability of the lateral structures of residual flows (rather than the variability of the velocity profiles at each mooring separately). The data were also detrended to enhance the main signal variability (Preisendorfer & Mobley, 1988; Wilks, 2011), although the overall results were unchanged without this step. Residual velocities were considered for 12 cells with normalized depths between 0.38 and 0.88 as the method requires no data gap. To clearly characterize the spring–neap variability of the signal, the records from M2C (Limited to 1 month) and from M1E (affected by local advection from salt marshes — see section "ADCP Observations at Transect 1") were excluded from the analysis. Notably, their inclusion does not alter the results. Therefore, at both transects, the PCA was applied to a matrix of axial residual velocities with dimensions of time versus 24 depth cells (corresponding to the concatenated 12 cells from each of the two ADCPs).

For the towed ADCP records, the lack of vertical eddy viscosity measurements excludes the identification of the residual flow components related to the ESCO mechanisms (see Cheng, 2014). Alternatively, the baroclinic (ν_{bc}) and barotropic (ν_{bt}) residual flow components were separated following Li et al. (1998). Neglecting tidal variations in turbulent mixing, the proposed method is applicable to observations at both neap and spring tides under weak river discharge (Q) and wind conditions. Assuming that the barotropic component is proportional to the tidal amplitude (a) at the mouth, and that the baroclinic component is a function of both the tidal forcing and river discharge, the following equations are derived:

$$v_{bt}^{n} = v_{bt}^{s}\frac{a^{n}}{a^{s}} \tag{1}$$

$$v_{bc}^{n} = v_{bc}^{s}\phi \tag{2}$$

$$v_{bt}^{s} = \frac{\phi v^{s} - v^{n}}{\phi - a^{n}/a^{s}} \tag{3}$$

$$v_{bc}^{s} = \frac{v^{n} - v^{s}a^{n}/a^{s}}{\phi - a^{n}/a^{s}} \tag{4}$$

in which the superscripts indicate neap (n) and spring (s) tides, and ϕ is a ratio defined as:

$$\phi = \frac{Q^{n}}{Q^{s}}/\frac{a^{n}}{a^{s}} \tag{5}$$

Equations (1) to (5) were computed considering the daily average river discharge at neap tide ($Q^n = 4.5$ m^3/s, with $a^n = 0.6$ m) and at spring tide ($Q^s = 6$ m^3/s, with $a^s = 1.5$ m) from the Pulo de Lobo hydrographic station (Fig. 1, inset).

Results

Observations

ADCP Observations at Transect 1

During the observation period, the daily averaged river discharge ranged between 2.5 and 8 m^3/s (Fig. 2a). Towed ADCP measurements near the mouth indicate a residual outflow across the section at spring tide and a two-layer exchange flow at neap tide, with residual velocities generally below 0.1 m/s (Fig. 2b, c). At spring tide, the outflow

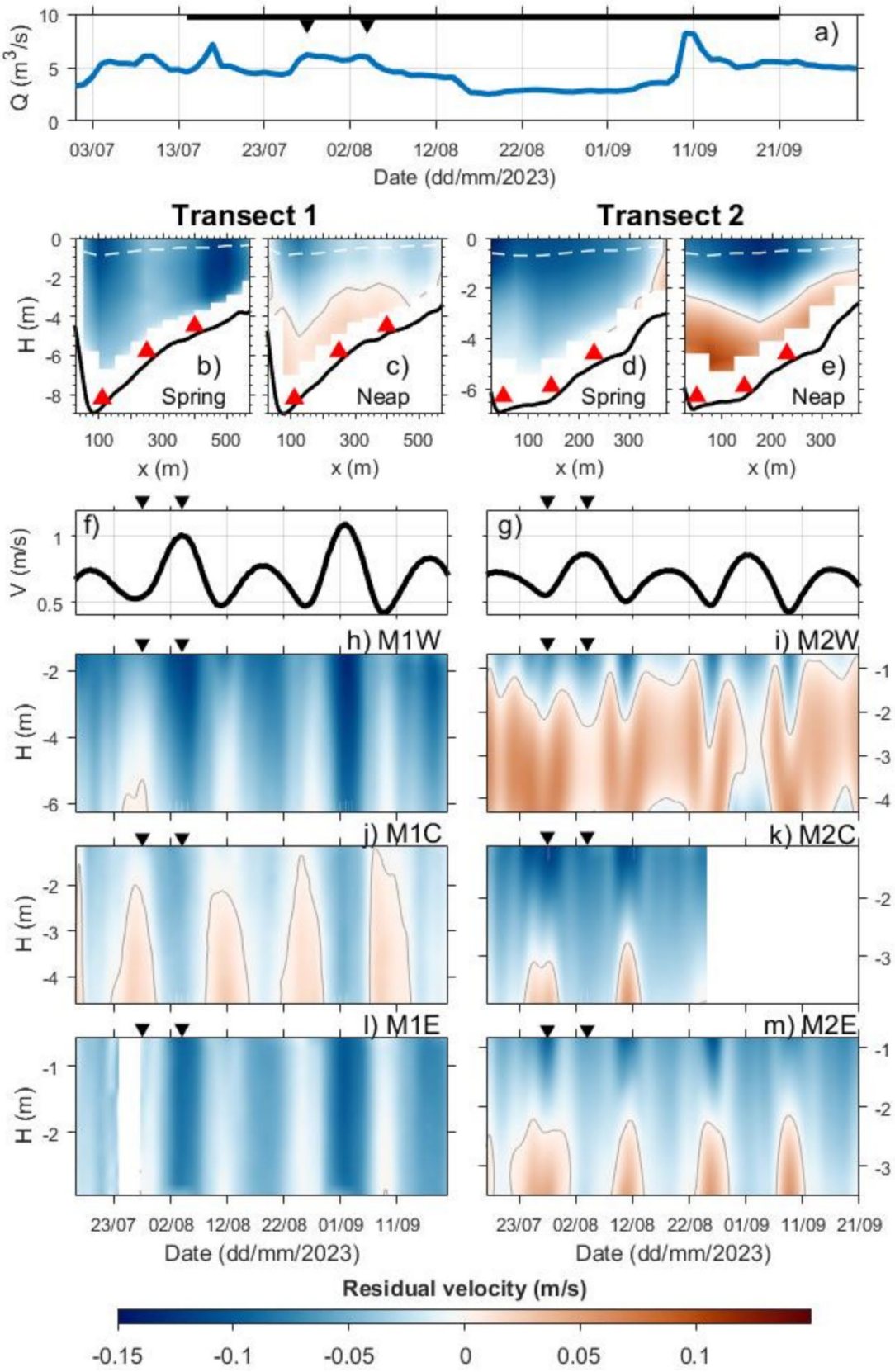
a)
Q (m3/s)
Date (dd/mm/2023)
Transect 1
Transect 2
b) Spring
c) Neap
d) Spring
e) Neap
H (m)
x (m)
f)
g)
V (m/s)
h) M1W
i) M2W
j) M1C
k) M2C
l) M1E
m) M2E
Residual velocity (m/s)

◂**Fig. 2** Residual axial flows (m/s, positive upstream in red, with the zero velocity contour line in grey) at Transect 1 (left column) and Transect 2 (right column): across the channel (*x*, distance from the west margin, m) at spring (**b**, **d**) and neap (**c**, **e**) tides, with indication of the approximate location of the ADCP moorings (red triangles) and of the uppermost valid cells (white dashed line); and at the deep (**h**, **i**), intermediate (**j**, **k**), and shallow (**l**, **m**) moorings with the tidal velocity amplitude at M1W (**f**) and M2W (**g**). The daily averaged river discharge (Q, m^3/s) from July to September 2023 is represented on top (**a**) with moored observations period as a tick black line. The black triangles indicate the time of the tidal surveys. For clarity, labels are shown only once for side-by-side plots with identical axes

was weakest in the middle of the transect (Fig. 2b). Accordingly, vertically averaged peak tidal currents were significantly stronger during the ebb than during the flood (by more than 10 cm/s), except in the middle of the section (Fig. 3, thick solid lines). Across the section, the peak ebb and flood currents were generally the strongest over the deep channel and progressively weaker eastward with decreasing water depth, due to bottom friction (see Fig. 3, thick lines, with the water depth as a dashed line). However, this typical pattern was not observed between 400 and 550 m, where peak ebb flows were locally enhanced despite the shallow water depth (Fig. 3, compare the thick blue line with the dashed line). With no sharp bathymetric variations in this area, the strengthening of the ebb flood flow during spring tide at the eastern part of the transect is attributed to the withdrawal of the water stored at high tide in the Ayamonte salt marsh, upstream of Transect 1 (Fig. 1a). In support, divers who were checking the moorings reported a sharp front of warmer and more turbid water when swimming from M1C to M1E. The strengthening of the ebb flow by the marsh withdrawal produced the residual outflow near the eastern margin at spring tide (Fig. 2a). In comparison, the smaller storage volume at neap tide resulted in a weaker influence on peak ebb flows (Fig. 3, thin lines). Nevertheless, the salt marsh withdrawal still produced a residual outflow near the east margin at neap tide, in contrast to the two-layer flow observed elsewhere along the transect (Fig. 2b).

At the time of the tidal surveys, residual velocities at the moorings also exhibited a two-layer exchange flow at neap tide (except at M1E, where data were unavailable) and an outflow at spring tide (Fig. 2h, j, l). This fortnightly variability was consistently observed at M1C throughout the observation period (Fig. 2j). In contrast, the two other moorings (M1W and M1E) generally revealed a unidirectional outflow throughout the water column, which was weakest at neap tide (Fig. 2h, l). The general absence of a near-bed inflow at neap tide is likely due to the depth of the lowest observations (approximately 6 m for M1W and 3 m for M1E), which is close to the upper limit of the inflow observed during the neap tidal survey (Fig. 2c, h, l). For instance, a small near-bed inflow was detected at M1E during the weakest tide, when the flow was the most developed at the adjacent mooring M1C (September 9 in Fig. 2j, l,).

At all three moorings, the strength of the residual flow increased with the tidal velocity amplitude (Fig. 4a). This relationship is Linear and well-defined for a tidal forcing exceeding 0.7 m/s, but more scattered under weaker tidal conditions. The relatively strong residual circulation at M1E (yellow dots) reflects the contribution of the Ayamonte salt marsh to the ebb flow.

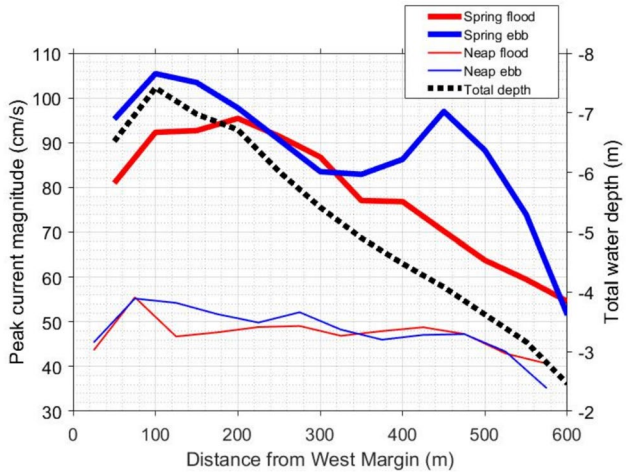

Fig. 3 Magnitude (cm/s) of peak flood (blue) and ebb (red) currents (vertically averaged) during spring (thick lines) and neap (thin lines) tides at Transect 1. The cross-section bathymetry (total water depth, m) is represented with a dashed black line on the right *y*-axis (note that the axis is reversed to highlight the correspondence with peak velocities)

ADCP Observations at Transect 2

The tidal current amplitude from Transects 1 to 2 was roughly constant at neap tide and slightly damped at spring tide (Fig. 2f, g). This pattern is in agreement with the previously described tidal wave dynamics induced by fortnightly variations in bottom friction along the seaward half of the estuary (Garel & Cai, 2018). At spring tide, a residual outflow occupied most of the cross-section at Transect 2, except for a localized inflow near the eastern margin (Fig. 2c). At neap tide, a two-layer exchange flow developed, with stronger magnitude (approximately 0.1 m/s) than at Transect 1 (Fig. 2c, e).

Residual velocities at moorings M2C and M2E (Fig. 2k, m) were consistent with the cross-channel structures described above. In contrast, a persistent two-layer flow was generally observed at M2W, with a near surface outflow generally confined to the upper 2 m (Fig. 2i). A near-bed outflow tended to grow upward at spring tide, eventually occupying the entire water column during the strongest spring tide on September 1.

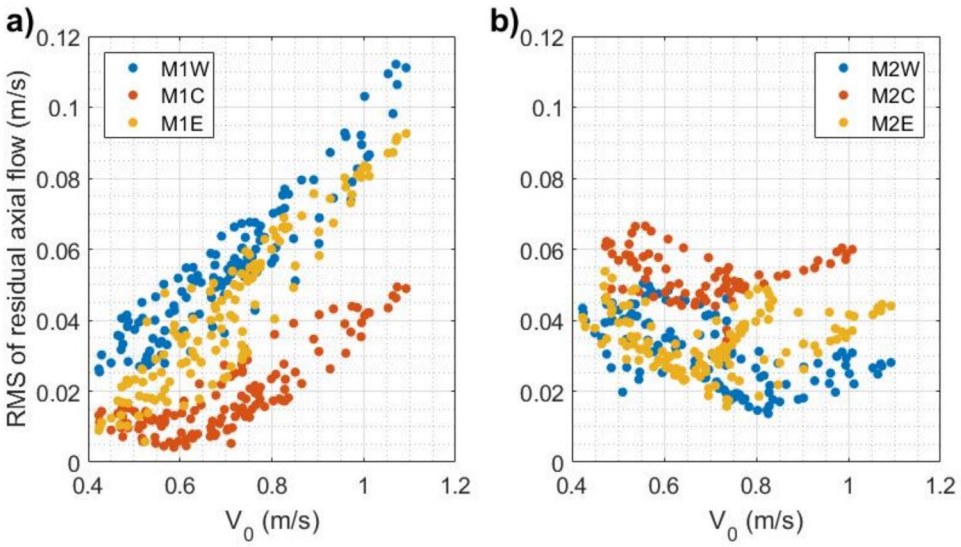

Fig. 4 Root mean square (rms) of axial residual velocity profiles (m/s) as a function of the tidal velocity amplitude at the mouth (V_0, m/s) for moorings W (blue), C (red), and E (yellow) at Transects 1 (**a**) and 2 (**b**)

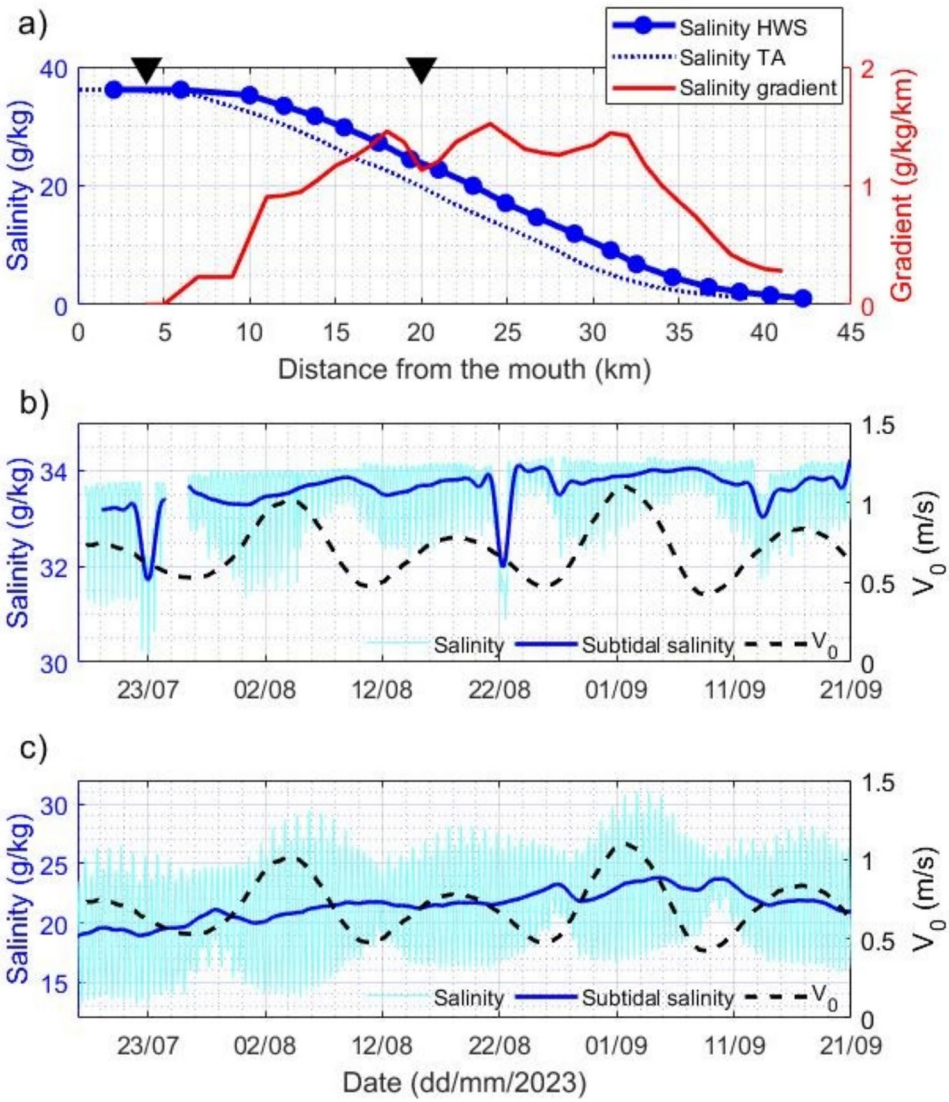

Fig. 5 Salinity measurements (in g/kg) at the Guadiana Estuary in summer 2023: **a** left axis: salinity (vertical mean) on 11 July 2023 along the channel (km) at high-water slack (solid blue line with dots indicating the measurement locations) and tidally averaged (dotted line); right axis (red line): salinity gradient (g/kg/km) at high-water slack; the black triangles on top indicate the two transect locations; **b**, **c** left axis: tidal (light cyan line) and low-pass-filtered (solid blue line) near-bed salinity at 4 km (**b**) and 20 km (**c**) from the mouth; right axis (dashed line): tidal velocity amplitude at M1W (V_0, m/s)

The residual circulation at Transect 2 was generally weaker during spring tide and stronger during neap tide compared with Transect 1 (Fig. 4). Moreover, the residual flow intensity at the three moorings exhibited a negative relationship with tidal amplitude below approximately 0.8 m/s (Fig. 4b). Above this threshold, the relationship reversed as residual flows strengthened with increasing tidal amplitude, as observed at Transect 1.

Salinity

Along-channel salinity variations exhibited a sigmoid shape, with an intrusion length of 42 km at high-water slack (Fig. 5a, solid blue line). Seawater (i.e. defined as salinity ≥ 35 g/kg) was observed up to 10 km from the mouth, corresponding to a tidal average intrusion of 7 km (Fig. 5a, dotted line). Consequently, the horizontal salinity gradient was relatively weak (< 1 g/kg/km) at the lower estuary (Fig. 5a, red line). The stratification parameter (i.e. the bottom to surface salinity difference normalized by the vertical average salinity) ranged between 0 and 0.07 (not shown), indicating well-mixed conditions (Prandle, 1985) for a tidal amplitude of 0.75 m, at least at high-water slack.

Tidal salinity variations recorded by the moored CTDs were relatively small near the mouth (about 2 g/kg) but larger upstream (reaching about 10 g/kg; Fig. 5b, c, cyan lines). Episodic salinity drops at M1E (e.g. on July 23 in Fig. 5b) suggest freshwater inputs of unknown origin (not accounted for by river discharge records). Generally, the phase shifts at both moorings between salinity variations and current amplitude, where salinity leads by about 4 days at M1E and lags by about 2 days at M2W, points to an intricate salt dynamics along the estuary.

At the subtidal timescale, the salinity increased by approximately 0.5 g/kg near the mouth and 5 g/kg upstream between mid-July and September 9 (Fig. 5b, c, thick blue lines). During this period, the salinity difference between the two stations decreased by about 4.5 g/kg, indicating a landward extension of the salinity intrusion. At the upstream station, a subtidal increase of ~ 1–2 g/kg in near-bed salinity during neap tides suggests enhanced water column stratification under weak tidal forcing conditions (Fig. 5c, thick blue line). No additional clear pattern of salinity variability was observed at the fortnightly timescale.

Baroclinic and Barotropic Flow Components

Moored ADCP

At Transect 1, the first two principal components explain 98% of the variability of the axial residual flow, with a large dominance of the variance explained by PC1 (92%, against 6% for PC2). The velocity profiles associated with both components are unidirectional at the two moorings (Fig. 6a, b). There is no significant contribution of a two-layer sheared flow in the signal variability. The amplitudes of PC1 are linearly related to the tidal current amplitude (Fig. 6c, blue dots), whereas PC2 remains relatively weak and shows no dependence with tidal forcing (Fig. 6c, red dots). These results indicate that residual flows at Transect 1 are primarily driven by the variability in the barotropic boundary layer.

At Transect 2, PC1 and PC2 together account for 90% of the signal variability. At both moorings, PC1 exhibits a unidirectional vertical profile, while PC2 displays an exchange flow, characteristic of the gravitational circulation with a pronounced vertical shear (top-to-bottom velocity difference of approximately 0.6 m/s; Fig. 6d, e). Compared to Transect 1, PC2 at Transect 2 explains a large part of the signal variability (53% for PC1, 37% for PC2) and shows a similar order of magnitude than PC1 (Fig. 6f). Notably, the trends of PC1 and PC2 velocities are related with the tidal forcing, with PC1 magnitude increasing and PC2 magnitude decreasing around the threshold of 0.7 m/s, approximately. These trends mirror the observed tidal variability in residual flow intensity at the moorings (Fig. 4b). PC1 dominates for large tidal current amplitudes, being strongest at spring tide, indicating that the residual circulation is primarily barotropic under these conditions, as at Transect 1. In contrast, PC2 becomes dominant under weaker tidal forcing (below ~ 0.7 m/s), particularly at neap tide, producing the observed vertically sheared residual circulation (e.g. Figure 2e). These results suggest that the dominant mechanism driving the residual circulation at Transect 2 shifts with the tidal forcing.

Towed ADCP

The method to separate the barotropic and baroclinic residual flow from the towed ADCP data assumes a proportionality of both components to tidal forcing (see Eqs. 2 and 5). This assumption is supported by the present PCA results, which show that the barotropic profile and exchange flow (detected only at Transect 2) are enhanced with decreasing and increasing tidal forcing, respectively (Fig. 6c, f). The results show, for both transects, a similar lateral structure of each flow component at neap and spring tides, but with differing magnitudes, due to the linear relationships expressed in Eqs. 1 and 5. The barotropic component corresponds to a general unidirectional outflow that is strongest at spring tide, while the baroclinic component is vertically sheared and strongest at neap tide (Fig. 7). The barotropic flow structure is closely similar to the residual circulation observed at spring tide (Fig. 2a, c), including the inflow at the eastern end of Transect 2. The outflow observed near the eastern margin of Transect 1 is also present in the barotropic component, consistent with ebb flow advection from the salt

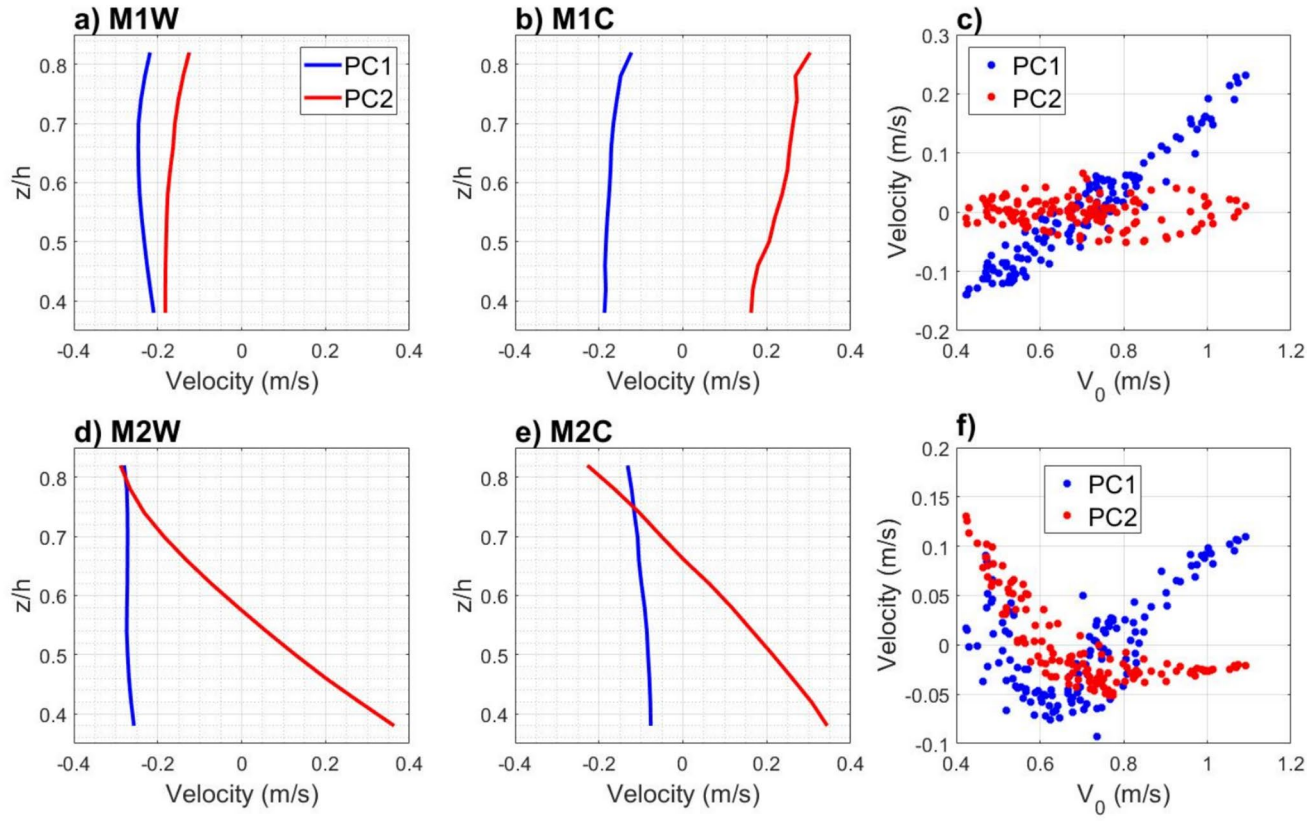

Fig. 6 Vertical velocity profiles of PC1 (blue) and PC2 (red) at M1W (**a**), M1C (**b**), M2W (**d**), and M2E (**e**). Time variability of PC1 and PC2 vs tidal current amplitude at M1W (V_0, m/s) at Transects 1 (**c**) and 2 (**f**)

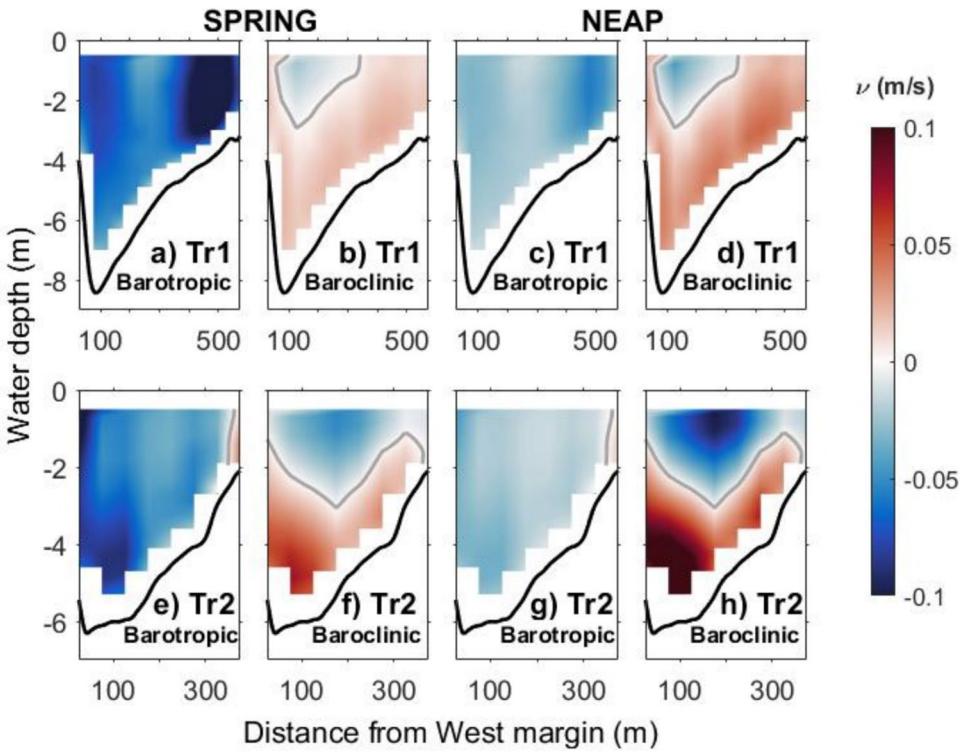

Fig. 7 Axial residual flow components (v, m/s) across the channel. Barotropic (**a**, **c**, **e**, **g**) and baroclinic (**b**, **d**, **f**, **h**) components at Transects 1 (upper) and 2 (lower) at spring (**a**, **b**, **e**, **f**) and neap (**c**, **d**, **g**, **h**) tides. The zero-contour line is indicated in grey

marsh due to a phase lag in water level between the marsh and the estuarine channel. The baroclinic structure mimics the observations at neap tide (Fig. 2b, d), characterized by an exchange flow that is notably stronger at transect 2 than at Transect 1 (compare Fig. 7b, f with Fig. 7d, h).

Discussion

Evidence for Driver Switching

Towed ADCP observations across two channel sections of the Guadiana Estuary reveal a striking fortnightly switch in the lateral structure of axial residual currents. Specifically, a two-layer, vertically sheared, exchange flow was observed at neap tide while a section-wide outflow developed at spring tide (Fig. 2a–d). A similar pattern was generally evident in the moored ADCP records (Fig. 2e–l). Exceptions were at M1W and M1E at neap tide (mainly outflow) and at M2W at spring tide (two-layer flow). The outflows at M1W and M1E are attributed to the large distance from the bed of the 1 st ADCP cell (at more than 30% of the water column). In support, previous long-term ADCP measurements nearby M1W — but closer to the bed — revealed the development of a near-bed inflow at neap tide that vanishes as the tidal amplitude increases (Garel & Ferreira, 2013). At M2W, the outflow clearly extends vertically when the tidal forcing is around spring tides, developing through the entire water column during the largest spring tide (Fig. 2h), indicating that the residual flow at the mooring tends to be consistent with the one from the tidal survey at spring tide. The discrepancy is attributed to the distinct local bathymetry between the M2W mooring and cross-channel survey, which were 150 m apart in a morphologically complex area with dynamic sand dunes and channel meandering.

A fortnightly variability of the lateral structure of residual flow is not commonly observed at estuaries, where the structure typically persists when external forcings other than tides are relatively constant (e.g. Geyer et al., 2000; Li & Zhong, 2009; Ross et al., 2017; Valle-Levinson et al., 2000b, 2009). The fortnightly variability observed herein suggests a switching of the dominant forcing mechanism, occurring at intermediate tidal current amplitudes of approximately 0.7–0.8 m/s based on moored observations (Fig. 2i, j, k, m).

Theoretical barotropic models considering a constant eddy viscosity predict that tidal stress in dynamically long and narrow estuaries, such as the Guadiana, produces a laterally sheared flow with outflow in the deep channel and inflows over the flanking shoals (Li & O'Donnell, 2005). At Transect 2, this lateral structure was observed at spring tide, although the inflow was restricted to the eastern end of the section ($x > 300$ m in Fig. 2c). The increasing vertical extent of this inflow with cross-channel distance suggests that it occupied the easternmost unsampled area, highlighting the difficulty to obtain residual velocities in shallow, meso- to macrotidal environments.

At Transect 1, a strong residual outflow (rather than the inflow predicted by tidally averaged barotropic models) was observed over the shallowest (eastern) area during spring tide (Fig. 2a). This outflow is a persistent pattern, systematically observed at M1E (Fig. 2k; Fig. 4a, yellow dots), and was also reported in previous cross-channel tidal surveys at this location (e.g. Teodósio & Garel, 2015). The atypically strong peak ebb velocities in this shallow area during spring tide (nearly matching those in the deep channel; Fig. 3), along with diver observations of a front between M1C and M1E, suggest that the residual outflow at East is produced by the outgoing jet from the Ayamonte salt marsh. With no freshwater inputs and a direct connection to the sea (Fig. 1), the marsh contains exclusively seawater. Thus, the relatively small tidal variations in salinity observed at M1E during spring tides (Fig. 5b) may also be explained by the addition of seawater into the estuarine channel during the ebb (e.g. MacVean & Stacey, 2011). This process is typically strongest during spring tides when the marshes experience the greatest inundation (Dronkers, 1979). Besides, peak ebb flows are strongest in the deep channel, while flood flows dominate in the shallower middle section of the channel ($x = 300$ m in Fig. 3), due to greater frictional effects at low tide than at high tide. It seems therefore that, in the absence of the Ayamonte salt marsh contribution, flood flows would also prevail over the shallower eastern area, where bed friction is even stronger, resulting in a residual inflow.

Based on the above observations, the residual flows at spring tide at both transects can reasonably be associated to the lateral structures produced by tidal stresses. In convergent mesotidal estuaries, these barotropic flows strengthen linearly with tidal forcing as non-linearities increase with tidal current amplitude (Ianniello, 1977, 1979; Kjerfve, 1986; Li et al., 1998). This pattern is consistent with the observed positive correlation between large (> 0.7 m/s) tidal amplitude and both the residual flow strength (Fig. 4) and the amplitude of the barotropic contribution PC1 (Fig. 6c, f, blue dots). This proportionality supports the assumption underlying the separation of barotropic (tidal stress) and baroclinic components in the residual circulation (Li et al., 1998). The resulting barotropic lateral structure (Fig. 7a) closely resembles the observed residual circulation during spring tide (Fig. 2a, c). In contrast, numerical studies indicate that the ESCO circulation may also intensify with the tidal current amplitude (Burchard et al., 2011; Cheng et al., 2010, 2013; Stacey et al., 2008), but it typically exhibits lateral flow structures similar to those produced by the baroclinic circulation (Burchard & Hetland, 2010; Dijkstra et al., 2017; Stacey et al., 2008; Wei et al., 2021). Altogether, these

findings suggest that tidal stress is the dominant driver of the residual circulation at both transects during spring tide.

The vertically sheared, exchange flow observed during neap tides at both transects is typical of both the gravitational circulation described by theoretical baroclinic solutions in non-rotational channels (Valle-Levinson, 2008) and the ESCO circulation when asymmetric tidal mixing is accounted for (Burchard & Hetland, 2010; Cheng et al., 2010, 2011, 2013; Dijkstra et al., 2017). Distinguishing between the gravitational and ESCO circulations requires turbulence measurements, which are not available in this study. Nevertheless, in contrast to the ESCO, the gravitational circulation tends to be strongest during neap tide, when stratification reduces momentum exchange between the surface and bottom layers of density-driven flows (Linden & Simpson, 1988; Nunes & Lennon, 1987; Nunes Vaz et al., 1989).

At Transect 1, the two-layer flow is not captured in the principal modes of the signal variability (Fig. 6a–c), indicating the absence of a steady gravitational circulation (Stacey et al., 2001, 2008). Furthermore, the lateral structure of the baroclinic flow (Fig. 7d) only weakly corresponds to the tidal survey observations (Fig. 2c). At locations with weak horizontal salinity gradients, as at Transect 1 (Fig. 5a), the vertically sheared residual circulation is predicted to result mainly from ESCO processes (Wei et al., 2021; Burchard & Hetland, 2010; Burchard et al., 2011). The possible dominance of ESCO mechanisms during neap tide is consistent with the observed positive relationship between residual flow intensity and tidal current amplitude below 0.7 m/s (Fig. 4a).

At Transect 2, the residual flow intensity increases as the relatively weak (< 0.7 m/s) tidal current amplitudes decrease (Fig. 4b), a pattern characteristic of baroclinic residual flows. This behaviour is remarkably similar to that of the baroclinic component (PC2), which dominates the residual flow variability at neap tide (Fig. 6f). Furthermore, the opposing trends of PC1 and PC2 with tidal forcing are consistent with the assumptions proposed by Li et al. (1998) to separate the barotropic component (proportional to the tidal forcing) from the baroclinic component (inversely proportional; see Eqs. 1–5). The method yields a baroclinic lateral structure that closely resembles the observed circulation during the neap tidal survey (Figs. 2e and 7h).

Overall, the results reveal a clear fortnightly variability in the lateral structure of the residual circulation at two transects in the Guadiana Estuary, indicating a shift in their dominant driver. During spring tide, the circulation at both transects appears to be primarily driven by tidal stress. At neap tide, it could result from ESCO mechanisms at Transect 1 or from baroclinic forcing at Transect 2. The identification of a potential fortnightly switch of driver up to 20 km upstream from an estuary mouth is a novel finding. The underlying causes of this temporal variability at the study site are explored in the following section.

Baroclinic vs Barotropic Dominance

The S_2/M_2 amplitude ratio at the Guadiana is 0.4, close to the average value for meso- to macrotidal shelves. For example, selecting from Piccioni et al. (2018) the 76 tidal gauges located on the western European shelf, the mean S_2/M_2 ratio is 0.35 with a standard deviation of 0.04. Thus, the switching of drivers at Transect 2 is not Linked to an unusual spring-neap variability at the Guadiana Estuary. Moreover, at spring tide, the Guadiana is mesotidal with current amplitude of the order of 1 m/s (Garel & Cai, 2018; Garel et al., 2009), a canonical value for estuaries where the gravitational (or ESCO) circulation dominates (Bruun & Gerritsen, 1960; Savenije, 2001). Clearly, the barotropic dominance during spring tides at the Guadiana is not due to extremely energetic tides, contrary to, for instance, the Chacao Channel in Chile (Cáceres et al., 2003). For regular tidal forcing, a barotropic residual circulation was reported at systems with negligible freshwater inputs, such as the mesotidal North inlet in South Carolina, USA (Kjerfve & Proehl, 1979). However, the only observed example in dynamically long channels with horizontal density gradients is near the entrance of the Mossoró estuary (Brazil) during the dry season (Valle-Levinson & Schettini, 2016). Both the Mossoró and Guadiana are trumpet-shaped estuaries, where the channel narrows markedly near the mouth but becomes almost prismatic upstream. The salinity distribution along these systems is characterized by a few-kilometre seawater intrusion reflected by the sigmoid (or bell) shape of the salinity distribution (Savenije, 2012), as observed in the present study (Fig. 5a) and from earlier measurements (e.g. Garel et al., 2018). Because of seawater intrusion, the horizontal density gradient is typically weak at the lower estuary, where salt transport is mostly due to tidal mixing (Savenije, 2012). The persistence of a weak gradient near the mouth is therefore consistent with the prevalence of barotropic forces (tidal advection at spring tide, and asymmetric tidal turbulence at neap tide) at Transect 1. Upstream (Transect 2), it is proposed that the weakening of baroclinic forcing due to seawater intrusion leads to the dominance of tidal stress in generating residual flows during spring tides.

To investigate further the competition between barotropic and baroclinic forces at Transect 2, the densimetric tidal Froude number (Fr_t) is computed based on observations. Fr_t is a dimensionless parameter proposed to diagnose whether the horizontal density gradient or tidal stresses are the dominant drivers of the residual circulation in estuaries (Valle-Levinson, 2021). It has been applied in various cases to support the switching of this driver with external forcing (discharge, tides) conditions (e.g. Ross et al., 2017; Tenorio-Fernandez et al., 2019; Valle-Levinson & Schettini, 2016).

Fr_t is computed as the ratio of the scaled tidal stresses (Nihoul & Ronday, 1975; Robinson, 1983; Zimmerman,

1978) and horizontal density gradient terms of the tidally averaged momentum equation:

$$Fr_t = \frac{L_\rho}{L_0}\frac{V^2}{Hg\Delta\rho/\rho_0} \quad (6)$$

In Eq. (6), V is the cross-channel mean tidal current amplitude at Transect 2; L_0 is the tidal length scale over which tidal mixing occurs along the channel, typically set to the tidal excursion; g is the acceleration caused by gravity; ρ_0 is a reference water density; H is the mean water depth (7 m at Transect 2); and L_ρ is a density length scale corresponding to the distance over which the along-channel density difference $\Delta\rho$ is considered. Fr_t is represented using a log-scale, where positive values indicate the prevalence of tidal stresses and negative values of the steady baroclinic forcing induced by the horizonal density gradient. Because it is based on the tidally averaged momentum equation, this approach does not account for the potential contribution of asymmetric tidal turbulence to the estuarine circulation. However, numerical studies have established that the ESCO circulation scales approximately linearly with the salinity gradient, similar to the gravitational circulation (Burchard & Hetland, 2010). Therefore, negative Fr_t values may also indicate a strong contribution of the ESCO circulation to the gravitational circulation.

First, Fr_t is computed with a density length scale of 30 km. This distance corresponds to the salinity intrusion length observed on July 11, over which salinity varies between 36 and 5 g/kg (Fig. 4a). In this case the baroclinic forcing that competes against tidal stress at Transect 2 results from the mean horizontal density gradient along the entire salty estuary, which is independent of the local along-channel salinity distribution.

The results indicate that the circulation is dominantly baroclinic for any tidal forcing (Fig. 8, black line). This is the typical situation described in the literature for well-mixed and partially stratified midlatitude estuaries (e.g. Geyer & MacCready, 2014). However, these results do not match the occurrence of a tidally driven circulation at spring tide at Transect 2.

In a second case, Fr_t is computed considering the distance between the two transects ($L_\rho = 16$ km). The horizontal density gradient (obtained from the axial salinity distribution on July 11) corresponds to the mean value between the two transects and is therefore more representative of the local salinity distribution than in the first case. In particular, the mean gradient between Transects 1 and 2 is 10 to 60% weaker than for the entire estuary (case 1) because of seawater intrusion (the salinity curve in the vicinity of Transect 1 is flat; Fig. 5a). In this second case, Fr_t successfully predicts the switching of driver with tidal forcing (Fig. 8, red line) that was reported at Transect 2. Alternatively, to account for the temporal variability of the density gradient, Fr_t is also computed using the density difference ($\Delta\rho$) obtained from the subtidal moored CTD records

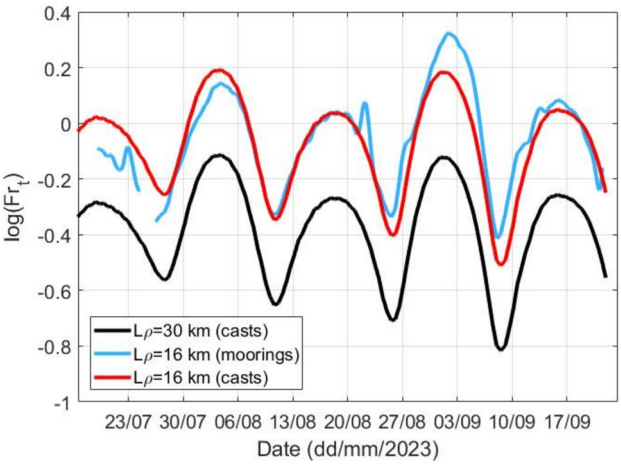

Fig. 8 Tidal Froude number (Fr_t) computed at Transect 2 using CTD data from either moorings or along-channel casts for $L_\rho = 30$ km (salinity intrusion length, black line) and $L_\rho = 16$ km (distance between Transects 1 and 2, blue and red lines)

(Fig. 4b, c), assumed to correspond to the section means. This assumption is corroborated by the weak (< 1 g/kg) lateral variability of salinity observed at both transects during the tidal surveys, with generally well-mixed conditions (except at slack ebb of the neap tide at Transect 2). The results closely match those derived from the along-channel CTD data (Fig. 8, blue line), supporting that the weakening of the horizontal density gradient by seawater intrusion can lead to tidal stress dominance along the lower stretch of estuaries, particularly during spring tides. At the Guadiana, this effect is Likely amplified by the fortnightly variability of the seawater intrusion, which is greater during spring tides than neap tides due to increased seawater advection from the Ayamonte salt marsh. For example, the tidally average intrusion was 6 km more upstream at spring than at neap during a drought period in Summer 2015 (unpublished data). Typically, the additional salt flux in the main channel alters the salinity field over a distance equal to the excursion length, while salinity gradients, advected both upstream and downstream, are affected over a distance twice as large (Garcia et al., 2022; MacVean & Stacey, 2011; van Keulen et al., 2025). For example, considering a spring tidal amplitude of 1 m/s, the tidal excursion is about 14 km along the Guadiana Estuary, while the salinity intrusion length is typically about 40 km (e.g. Figure 5a). In this situation, advection from the salt marsh may promote the dominance of tidal stress at spring tide along more than half of the salty estuary.

Conclusion

ADCP observations were performed simultaneously at two transects of the Guadiana Estuary to examine the variability of the residual flow drivers with tidal forcing. The

results from the moored and towed records were consistent, except for an episodic discrepancy in the deep channel of Transect 2, attributed to the distance between the mooring and cross-channel survey. At neap tide, a vertically sheared exchange flow was observed at both transects, typical of the gravitational and ESCO circulations. At spring tide, the circulation resembles the lateral exchange flow produced by tidal stress in barotropic models, even though the inflow over the shoals was masked by the additional seawater advection from salt marshes at Transect 1, and poorly developed at Transect 2. The modulation of the residual flow intensity with tides, along with PCAs and the separation of the barotropic and baroclinic flow components indicate that the circulation is mainly barotropic near the mouth, where it is hypothesized that an ESCO mechanism produces the vertical exchange flow at neap tide. Upstream, the same analyses demonstrate a switching of the main flow driver between neap tide (baroclinic with potential contributions of asymmetric tidal turbulences) and spring tide (barotropic, due to tidal stress). The occurrence of a switching of the dominant driver of the residual circulation with tidal forcing as far as 20 km from the mouth of a long and narrow estuary is a key finding of this study.

CTDs measurements show that seawater (with salinity > 35 g/kg) reaches several kilometres upstream the Guadiana, typical of trumpet-shaped estuaries. Over this seawater intrusion length, the horizontal density gradient is weak, supporting the predominance of tidally induced residual flows near the mouth. At 20 km from the mouth, a scaling analysis of the residual momentum equation (using the densimetric tidal Froude number) indicates that the weakening of the horizontal density gradient by seawater intrusion can lead to the creation of barotropic residual flows by tidal stress at spring tide, alternating with a gravitational circulation at neap tide (with potential contribution of the ESCO circulation).

The above results provide new insights about the fortnightly residual circulation at long and narrow midlatitude estuaries affected by a low river discharge. The main message is that the dominant driver can vary both temporally (spring — neap) and spatially (along the channel) due to the weakening of the horizontal density gradient by seawater intrusion. At the Guadiana, where a fortnightly switching of the residual drivers was reported as far as 20 km from the mouth, the storage of seawater over salt marshes probably enhances the seawater intrusion at spring tide, hence promoting the barotropic dominance. A detailed characterization of the salt dynamics along this estuary is required to further investigate this topic. For a generalization of the results, future research should investigate the residual flow dynamics at systems with large seawater intrusion due for example to a trumpet shape or to large seawater storage over salt marsh areas. The influence of seawater intrusion on the residual circulation is particularly relevant in the present context of increasing climate-related draughts.

Acknowledgements The authors are grateful to Enrique Padilla, André Pacheco, Luciano Júnior de Oliveira, Anja Rupp, Liliana Vasquez-Montoya and all the "Navios de Aviso" crew for their assistance during the field campaign. Thanks are extended to the Portuguese Environment Agency (APA, http://snirh.pt) for the provision of the water discharge data.

Author Contribution EG and AVL have designed the study. All authors have participated in the data acquisition, data processing, and discussions about the results. EG has written the paper which has been reviewed by all the co-authors.

Funding Open access funding provided by FCT|FCCN (b-on). The study was funded by the SWITCH project (PTDC/CTA-OHR/4268/2021) funded by the Portuguese Foundation for Science and Technology (FCT). The funding provided by FCT to projects LA/P/0069/2020 awarded to the Associate Laboratory "Aquatic Research Network" (ARNET) and UID/00350/2020 awarded to the Centre for Environmental and Marine Research (CIMA) of the University of Algarve are acknowledged.

Data Availability The observational dataset presented in the current study is available from the corresponding author.

Declarations

Ethics Approval and Consent to Participate Not applicable.

Consent for Publication Not applicable.

Competing Interests A. Valle-Levinson is an associate editor of *Estuaries and Coasts*. The other authors have no competing interest to disclose.

References

Arnott, K. D., Valle-Levinson, A., & Luther, M. (2012). Friction dominated exchange in a Florida estuary. *Estuarine, Coastal and Shelf Science, 113*, 248–258.

Basdurak, N. B., & Valle-Levinson, A. (2013). Tidal variability of lateral advection in a coastal plain estuary. *Continental Shelf Research, 61–62*, 85–97.

Bruun, P., & Gerritsen, F. (1960). Stability of coastal inlets. *Transactions of the American Society of Civil Engineers, 125*, 1228–1259.

Burchard, H., & Hetland, R. D. (2010). Quantifying the contributions of tidal straining and gravitational circulation to residual circulation in periodically stratified tidal estuaries. *Journal Of Physical Oceanography,40*, 1243–1262.

Burchard, H., Hetland, R. D., Schulz, E., & Schuttelaars, H. M. (2011). Drivers of residual estuarine circulation in tidally energetic estuaries: Straight and irrotational channels with parabolic cross section. *Journal of Physical Oceanography, 41*, 548–570.

Burchard, H., & Schuttelaars, H. M. (2012). Analysis of tidal straining as driver for estuarine circulation in well-mixed estuaries. *Journal of Physical Oceanography, 42*, 261–271.

Cáceres, M., Valle-Levinson, A., & Atkinson, L. (2003). Observations of cross-channel structure of flow in an energetic tidal channel. *Journal of Geophysical Research,108*, Article Article 3114.

Chant, R. J. (2002). Secondary circulation in a region of flow curvature: Relationship with tidal forcing and river discharge. *Journal of Geophysical Research,107*, Article 11.

Chawla, A., Jay, D. A., Baptista, A. M., Wilkin, M., & Seaton, C. (2008). Seasonal variability and estuary-shelf interactions in circulation dynamics of a river-dominated estuary. *Estuaries and Coasts, 31*, 269–288.

Cheng, P. (2014). Decomposition of residual circulation in estuaries. *Journal of Atmospheric and Oceanic Technology, 31*, 698–713.

Cheng, P., de Swart, H. E., & Valle-Levinson, A. (2013). Role of asymmetric tidal mixing in the subtidal dynamics of narrow estuaries. *Journal of Geophysical Research. Oceans, 118*, 2623–2639.

Cheng, P., & Valle-Levinson, A. (2009). Influence of lateral advection on residual currents in microtidal estuaries. *Journal of Physical Oceanography, 39*, 3177–3190.

Cheng, P., Valle-Levinson, A., & de Swart, H. E. (2010). Residual currents induced by asymmetric tidal mixing in weakly stratified narrow estuaries. *Journal of Physical Oceanography, 40*, 2135–2147.

Cheng, P., Valle-Levinson, A., & de Swart, H. E. (2011). A numerical study of residual circulation induced by asymmetric tidal mixing in tidally dominated estuaries. *Journal of Geophysical Research, 116*, Article C01017.

Correia, C., Torres, A. F., Rosa, A., Cravo, A., Jacob, J., de Oliveira Júnior, L., & Garel, E. (2020). Export of dissolved and suspended matter from the main estuaries in South Portugal during winter conditions. *Marine Chemistry, 224*, Article 103827.

de Jonge, V. N. (1992). Tidal flow and residual flow in the Ems estuary. *Estuarine, Coastal and Shelf Science, 34*, 1–22.

Dijkstra, Y. M., Schuttelaars, H. M., & Burchard, H. (2017). Generation of exchange flows in estuaries by tidal and gravitational eddy viscosity-shear covariance (ESCO). *Journal of Geophysical Research: Oceans, 122*, 4217–4237.

Dronkers, J. (1979). Longitudinal dispersion in shallow well-mixed estuaries. *Coastal Engineering,* pp. 2761–2777.

Fischer, H. B. (1976). Mixing and dispersion in estuaries. *Annual Review of Fluid Mechanics, 8*, 107–133.

Garcia, A. M. P., Geyer, W. R., & Randall, N. (2022). Exchange flows in tributary creeks enhance dispersion by tidal trapping. *Estuaries and Coasts, 45*, 363–381.

Garel, E. (2017). Collection and dissemination of data from environmental monitoring systems in estuaries. In *2017 4th Experiment@ International Conference* (exp.at'17), 61–64.

Garel, E., & Cai, H. (2018). Effects of tidal-forcing variations on tidal properties along a narrow convergent estuary. *Estuaries and Coasts, 41*, 1924–1942.

Garel, E., & D'Alimonte, D. (2017). Continuous river discharge monitoring with bottom-mounted current profilers at narrow tidal estuaries. *Continental Shelf Research, 133*, 1–12.

Garel, E., & Ferreira, Ó. (2013). Fortnightly changes in water transport direction across the mouth of a narrow estuary. *Estuaries and Coasts, 36*, 286–299.

Garel, E., Martins, F., Janeiro, J., & Oliveira, L.J.d. (2018). Relatório Intrusão Salina, Plano Intermunicipal de adaptação às alterações climáticas da AMAL (PIAAC-AMAL). Relatório técnico da fase 1: Identificação e avaliação de vulnerabilidades atuais, p. 467.

Garel, E., Pinto, L., Santos, A., & Ferreira, Ó. (2009). Tidal and river discharge forcing upon water and sediment circulation at a rock-bound estuary (Guadiana estuary, Portugal). *Estuarine, Coastal and Shelf Science, 84*, 269–281.

Geyer, W. R., Trowbridge, J. H., & Bowen, M. M. (2000). The dynamics of a partially-mixed estuary. *Journal of Physical Oceanography,30*, 2035–2048.

Geyer, W. R., & MacCready, P. (2014). The estuarine circulation. *Annual Review of Fluid Mechanics, 46*, 175–197.

Hansen, D. V., & Rattray, M., Jr. (1966). New dimensions in estuary classification 1. *Limnology and Oceanography,11*, 319–326.

Huijts, K. M. H., Schuttelaars, H. M., de Swart, H. E., & Friedrichs, C. T. (2009). Analytical study of the transverse distribution of along-channel and transverse residual flows in tidal estuaries. *Continental Shelf Research, 29*, 89–100.

Huntley, H. S., & Ryan, P. (2018). Wind effects on flow patterns and net fluxes in density-driven high-latitude channel flow. *Journal of Geophysical Research. Oceans,123*, 305–323.

Ianniello, J. (1977). Tidally induced residual currents in estuaries of variable breadth and depth. *Journal of Physical Oceanography, 9*, 962–974.

Ianniello, J. P. (1979). Tidally induced residual currents in estuaries of variable breadth and depth. *Journal of Physical Oceanography, 9*, 962–974.

Jay, D. A., & Musiak, J. D. (1994). Particle trapping in estuarine tidal flows. *Journal of Geophysical Research: Oceans, 99*, 20445–20461.

Kasai, A., Hill, A. E., Fujiwara, T., & Simpson, J. H. (2000). Effect of the Earth's rotation on the circulation in regions of freshwater influence. *Journal of Geophysical Research. Oceans,105*, 16961–16969.

Kim, Y. H., & Voulgaris, G. (2005). Effect of channel bifurcation on residual estuarine circulation: Winyah Bay, South Carolina. *Estuarine, Coastal and Shelf Science, 65*, 671–686.

Kjerfve, B. (1986). Circulation and salt flux in a well mixed estuary. In J. van de Kreeke (Ed.), *Lecture Notes on Coastal and Estuarine Studies*. Physics of shallow estuaries and bays, pp. 22–29.

Kjerfve, B., & Proehl, J. A. (1979). Velocity variability in a cross-section of a well-mixed estuary. *Journal of Marine Research,37*, 409–418.

Lerczak, J. A., & Geyer, R. W. (2004). Modeling the lateral circulation in straight, stratified estuaries. *Journal of Physical Oceanography,34*, 1410–1428.

Li, C., & O´Donnell, J. (1997). Tidally driven residual circulation in shallow estuaries with lateral depth variation. *Journal of Geophysical Research, 102*, 27915–27929.

Li, C. Y., & O'Donnell, J. (2005). The effect of channel length on the residual circulation in tidally dominated channels. *Journal of Physical Oceanography, 35*, 1826–1840.

Li, C., Valle-Levinson, A., Wong, K. C., & Lwiza, K. M. M. (1998). Separating baroclinic flow from tidally induced flow in estuaries. *Journal of Geophysical Research,103*(C5), 10405–10417.

Li, M., & Zhong, L. (2009). Flood-ebb and spring-neap variations of mixing, stratification and circulation in Chesapeake Bay. *Continental Shelf Research, 29*, 4–14.

Linden, P. F., & Simpson, J. E. (1988). Modulated mixing and frontogenesis in shallow seas andestuaries. *Continental Shelf Research, 8*, 1107–1127.

MacVean, L. J., & Stacey, M. T. (2011). Estuarine dispersion from tidal trapping: A new analytical framework. *Estuaries and Coasts, 34*, 45–59.

Morales, J. A. (1997). Evolution and facies architecture of the mesotidal Guadiana River delta (S.W. Spain-Portugal). *Marine Geology, 138*, 127–148.

Morales, J. A., & Garel, E. (2019). The Guadiana River Delta. In J. A. Morales (Ed.), *The Spanish coastal systems: Dynamic processes, sediments and management* (p. 823). Springer International Publishing.

Murphy, P., Waterhouse, A., Hesser, T., Penko, A., & Valle-Levinson, A. (2009). Subtidal flow and its variability at the entrance to a subtropical lagoon. *Continental Shelf Research,29*, 2318–2332.

Nihoul, J. C., & Ronday, F. C. (1975). The influence of the "tidal stress" on the residual circulation. *Tellus, 27*, 484–490.

Nunes, R. A., & Lennon, G. W. (1987). Episodic stratification and gravity currents in a marineenvironment of modulated turbulence. *Journal of Geophysical Research, 92*, 5465–5480.

Nunes Vaz, R. A., Lennon, G. W., & de Silva Samarasinghe, J. R. (1989). The negative role of turbulence in estuarine mass transport. *Estuarine, Coastal and Shelf Science, 28*, 361–377.

Piccioni, G., Dettmering, D., Bosch, W., & Seitz, F. (2018). TICON: Tidal constants based on GESLA sea-level records from globally distributed tide gauges (data). In Supplement to: Piccioni, G et al. (2019): TICON: TIdal CONstants based on GESLA sea-level records from globally located tide gauges. Geoscience Data Journal, 6(2), 97-104. https://doi.org/10.1002/gdj3.72 : PANGAEA.

Prandle, D. (1985). On salinity regimes and the vertical structure of residual flows in narrow tidal estuaries. *Estuarine, Coastal and Shelf Science, 20*, 615–635.

Preisendorfer, R. W., & Mobley, C. D. (1988). *Principal component analysis in meteorology and oceanography*. Elsevier; Distributors for the U.S. and Canada, Elsevier Science Pub. Co.

Pritchard, D. W. (1956). The dynamic structure of a coastal plain estuary. *Journal of Marine Research, 15*, 33–42.

Reyes, C., & Valle-Levinson, A. (2013). Fortnightly variations of the lateral structure of flow and hydrography at the Chesapeake Bay entrance. *Continental Shelf Research, 52*, 46–61.

Robinson, I. S. (1983). Tidally induced residual flows. In B. Johns (Ed.), *Elsevier Oceanography Series* (Vol. 35, pp. 321–356). Elsevier.

Ross, L., Valle-Levinson, A., Sottolichio, A., & Huybrechts, N. (2017). Lateral variability of subtidal flow at the mid-reaches of a macrotidal estuary. *Journal of Geophysical Research-Oceans,122*, 7651–7673.

Savenije, H. H. G. (2001). A simple analytical expression to describe tidal damping or amplification. *Journal of Hydrology, 243*, 205–215.

Savenije, H. H. G. (2012). *Salinity and tides in alluvial estuaries*. Delft University of Technology.

Scully, M. E., & Friedrichs, C. T. (2007). The importance of tidal and lateral asymmetries in stratification to residual circulation in partially mixed estuaries. *Journal of Physical Oceanography, 37*, 1496–1511.

Scully, M. E., Friedrichs, C. T., & Brubaker, J. M. (2005). Control of estuarine stratification and mixing by wind-induced straining of the estuarine density field. *Estuaries and Coasts,28*, 321–326.

Stacey, M. T., Burau, J. R., & Monismith, S. G. (2001). Creation of residual flows in a partially stratified estuary. *Journal of Geophysical Research,106*, 17013–17043.

Stacey, M. T., Fram, J. P., & Chow, F. K. (2008). Role of tidally periodic density stratification in the creation of estuarine subtidal circulation. *Journal of Geophysical Research: Oceans*. https://doi.org/10.1029/2007JC004581

Tenorio-Fernandez, L., Zavala-Hidalgo, J., & Olvera-Prado, E. R. (2019). Seasonal variations of river and tidal flow interactions in a tropical estuarine system. *Continental Shelf Research, 188*, Article 103965.

Teodósio, M. A., & Garel, E. (2015). Linking hydrodynamics and fish larvae retention in estuarine nursery areas from an ecohydrological perspective. *Ecohydrology & Hydrobiology,15*, 182–191.

Valle-Levinson, A. (2008). Density-driven exchange flow in terms of the Kelvin and Ekman numbers. *Journal of Geophysical Research*. https://doi.org/10.1029/2007JC004144

Valle-Levinson, A. (2021). Dynamics-based classification of semienclosed basins. *Regional Studies in Marine Science, 46*, Article 101866.

Valle-Levinson, A. (2022). *Introduction to estuarine hydrodynamics*. Cambridge University Press.

Valle-Levinson, A. (2024). 2.9 - Collection and processing of underway, bottom-tracking ADCP data. In D. Baird & M. Elliott (Eds.), *Treatise on estuarine and coastal science* (2nd ed., pp. 207–218). Academic Press.

Valle-Levinson, A., & Atkinson, L. P. (1999). Spatial gradients in the flow over an estuarine channel. *Estuaries, 22*, 179–193.

Valle-Levinson, A., Moraga, J., Olivares, J., & Blanco, J. L. (2000). Tidal and residual circulation in a semi-arid bay: Coquimbo Bay, Chile. *Continental Shelf Research, 20*, 2009–2028.

Valle-Levinson, A., Reyes, C., & Sanay, R. (2003). Effects of bathymetry, friction, and rotation on estuary–ocean exchange. *Journal of Physical Oceanography, 33*, 2375–2393.

Valle-Levinson, A., & Schettini, C. A. F. (2016). Fortnightly switching of residual flow drivers in a tropical semiarid estuary. *Estuarine, Coastal and Shelf Science, 169*, 46–55.

Valle-Levinson, A., Schettini, C. A. F., & Truccolo, E. C. (2019). Subtidal variability of exchange flows produced by river pulses, wind stress and fortnightly tides in a subtropical stratified estuary. *Estuarine, Coastal and Shelf Science, 221*, 72–82.

Valle-Levinson, A., Velasco, GGd., Trasviña, A., Souza, A. J., Durazo, R., & Mehta, A. J. (2009). Residual exchange flows in subtropical estuaries. *Estuaries and Coasts, 32*, 54–67.

Valle-Levinson, A., Wong, K.-C., & Lwiza, K. M. M. (2000). Fortnightly variability in the transverse dynamics of a coastal plain estuary. *Journal of Geophysical Research-Oceans,105*, 3413–3424.

van Keulen, D., Kranenburg, W. M., & Hoitink, A. J. F. (2025). Tidal trapping and its effect on salinity dispersion in well-mixed estuaries revisited. *Estuaries and Coasts*: In press.

Wei, X., Schuttelaars, H. M., Williams, M. E., Brown, J. M., Thorne, P. D., & Amoudry, L. O. (2021). Unraveling interactions between asymmetric tidal turbulence, residual circulation, and salinity dynamics in short, periodically weakly stratified estuaries. *Journal of Physical Oceanography, 51*, 1395–1416.

Wilks, D.S. (2011). *Statistical methods in the atmospheric sciences*. Elsevier Science.

Winant, C. D. (2004). Three-dimensional wind-driven flow in an elongated, rotating basin. *Journal of Physical Oceanography, 34*, 462–476.

Winant, C. D. (2008). Three dimensional residual tidal circulation in an elongated, rotating, basin. *Journal of Physical Oceanography,38*, 1278–1295.

Winant, C. D., & Gutiérrez de Velasco, G. (2003). Tidal dynamics and residual circulation in a well-mixed inverse estuary. *Journal of Physical Oceanography, 33*, 1365–1379.

Wong, K. C. (1994). On the nature of transverse variability in a coastal plain estuary. *Journal of Geophysical Research,99*(C7), 14209–14222.

Zimmerman, J. T. F. (1978). Topographic generation of residual circulation by oscillatory (tidal) currents. *Geophysical and Astrophysical Fluid Dynamics, 11*, 35–47.